

<https://doi.org/10.1038/s41545-024-00304-x>

Air-gap-assisted solvothermal process to synthesize unprecedented graphene-like two-dimensional TiO₂ nanosheets for Na⁺ electrosorption/desalination

Billel Salhi¹, Nadeem Baig ¹ & Ismail Abdulazeez¹

Designing a high-performance capacitive deionization setup is limited due to the slow salt removal and charge storage capacities. Efforts are being made to replace traditional electrodes with advanced 2D materials. We introduce a simple method for synthesizing two-dimensional titanium dioxide graphene-like nanosheets via a unique air-gap-assisted solvothermal method. Crystalline 2D graphene-like anatase-TiO₂ sheets of unprecedented quality were obtained by tuning the air gap in the solvothermal reactor. The 2D TiO₂ synthesized by air-gap-assisted solvothermal process has shown an exceptionally high surface area of 934.5 m²/g compared to the pristine TiO₂ (249.5 m²/g). The sheets were used as Faradaic electrodes in ion-electrosorption and their capacitive deionization capabilities were evaluated. The electrochemical conductivity was examined via an in situ investigation of Na⁺-ion migration and storage. The adsorption capacity of 2D TiO₂ sheets increased with higher applied potential while keeping the adsorption time constant at 15 min. At adsorption potentials of -0.8 V, -1.0 V, and -1.2 V, desalting rates of 2.09, 2.18, and 2.20 mg g⁻¹ min⁻¹ resulted in adsorption capacities of 31.33, 32.73, and 33.023 mg g⁻¹, respectively. The 2D TiO₂ electrode demonstrated high electron-transfer rates, a large desalination capacity, and a rapid average desalting rate. The specific capacity of the 2D-layered TiO₂ electrode was found to be about 45.68 F g⁻¹. These results can be attributed to the large specific surface area, short ionic diffusion paths, numerous active adsorption sites, surface defects, and pseudocapacitance. This air-gap-assisted solvothermal method is expected to open new avenues for the synthesis of high-quality 2D materials.

Water shortage has emerged as a major worldwide concern, with 17 nations currently experiencing high water stress and utilizing more than 80% of their available supply annually. This number is expected to increase to 33 nations by 2040¹. Therefore, developing water scarcity mitigation techniques is urgently needed. Given that more than 97 percent of Earth's water is saline, desalination of seawater or brackish water is a potentially viable method for ensuring a sustainable freshwater supply². Desalination methods, including reverse osmosis (RO), electrodialysis (ED), multistage flash, and multi-effect distillation, have improved rapidly in recent years^{3,4}. Water-stressed countries, notably those in the Middle East, have embraced this technology, with Saudi Arabia relying on desalination for more than 70% of

its freshwater supply. Meanwhile, traditional desalination processes are extremely energy-intensive^{1,2}. RO requires a high osmotic pressure (1–10 MPa) for salt separation and is associated with membrane fouling problems^{5,6}. Thermal desalination procedures require a large amount of heat for water vaporization and are frequently limited by equipment corrosion^{1,2}. Extremely high voltages (>20 V) are used in ED to promote ion mobility for separation, which may result in water breakdown^{3,7}. Therefore, new high-efficiency desalination methods that are energy-efficient and ecologically benign are urgently needed.

Owing to its energy efficiency, cost-effectiveness, and eco-friendliness, capacitive deionization (CDI) has emerged as a promising desalination

¹Interdisciplinary Research Centre for Membranes and Water Security, King Fahd University of Petroleum and Minerals Dhahran, Dhahran 31261, Saudi Arabia.

e-mail: nadeembaig@kfupm.edu.sa

technique in recent years^{8,9}. In principle, the CDI is explained by the adsorption and desorption processes on the electrode surface under the influence of electrostatic force. The salt ions are adsorbed on the charged electrode surface, forming the electrical double layer¹⁰. The electrode surface can be regenerated easily just by reversing the polarity. During the regeneration process, the ions desorb from the electrode surface, and the surface becomes ready for the next cycle. The electrode material plays a central role in the CDI. Thus, the major research is focused on developing an electrode material that offers greater electrochemical stability, excellent electrical conductivity, good wettability, and high capacitance¹¹. CDI systems can function at low pressures (subosmotic) and ambient temperatures while using a low applied cell voltage (2 V). CDI selectively removes the minority salt ions from the saline solution rather than the majority water, making it suitable for efficiently desalinating low-salinity streams such as brackish water, which typically contains total dissolved salts (TDS) ranging from 1 g L⁻¹ to 10 g L⁻¹ (compared to seawater TDS of 35 g L⁻¹)^{2,12}. CDI consumes only 0.13–0.59 kW h m⁻³ for brackish water desalination. This is much lower than that of RO, the most energy-efficient classical desalination technique, which consumes 3.5–4.5 kW h m⁻³¹³. The electrode material affects the CDI performance considerably, as indicated by the variables. The role of electrode materials in desalination can be understood by focusing on ion capture mechanisms¹⁴. Electrosorption and Faradaic reactions are the two primary ion capture processes in CDI. Electrosorption occurs in standard CDI cells with carbon electrodes, where the potential difference is responsible for the adsorption of salt ions with opposing charges from the solution onto the surface of the carbon materials^{8,15}. The Faradaic mechanism occurs in Faradaic materials and consists of several processes: insertion and conversion reactions, ion-redox-active moiety interactions, and charge compensation with a redox-active electrolyte¹⁶. In contrast to those used in electrosorption, Faradaic electrode materials capture ions via Faradaic processes that occur throughout the bulk material and extend beyond the surface.

The different materials at the nanoscale have received significant attention in various applications^{17–21}. Titanium dioxide (TiO₂), in its different polymorphs such as anatase and rutile, has been extensively investigated as a Faradaic electrode for CDI. Owing to the redox reactions involving Ti⁴⁺ and Ti³⁺ ions, TiO₂ offers desirable electrochemical characteristics. Using TiO₂ compounds as Faradaic electrodes in CDI capitalizes on their electrochemical properties and ability to reversibly incorporate and release sodium ions. These characteristics contribute to their potential as effective desalination and water treatment materials in CDI systems. TiO₂ has a variety of polymorphs, which are dictated by the configuration of its TiO₆ octahedra²², with Ti⁴⁺ ions linked to six O₂⁻ ions. The most prevalent TiO₂ polymorphs are anatase TiO₂, rutile TiO₂, TiO₂-B, and TiO₂-H²³. Among these polymorphs, anatase, and rutile TiO₂ have been intensively used as Faradaic electrodes in ion-electrosorption-based technologies, such as supercapacitors and CDI.

The use of anatase TiO₂ in CDI has been the subject of numerous studies, as shown by several research publications^{15,24–28}. Various studies have addressed several limitations such as low electronic conductivity and slow ion diffusion to improve the desalination performance of TiO₂. The production of nanosized TiO₂²⁶ and the fusion of TiO₂ with carbon-based substrates such as hollow carbon fibers²⁶, activated carbon²⁹, graphene^{28,30}, and multiwalled carbon nanotubes (MWCNTs)^{27,31} are two methods that have been investigated in this area. Using a composite electrode composed of MWCNTs and TiO₂ nanotubes, Ramadan et al.²⁷ reported a salt-removal capacity of 13.2 mg g⁻¹ in a 50 mg L⁻¹ NaCl solution. Barakat et al.²⁴ developed a hybrid network electrode employing TiO₂ nanofibers and activated carbon, which reached a 17 mg g⁻¹ salt-removal capacity and an excellent 89.6% salt-removal efficiency in a 292 mg L⁻¹ NaCl solution. This study shows how nanoscale engineering and synergistic pairing with carbon-based materials can effectively enhance the desalination performance of TiO₂ in CDI. In addition to anatase TiO₂ mixed with carbon composites, the use of rutile TiO₂ in the form of carbon-embedded nanotubes for CDI applications was examined³². Rutile TiO₂ nanotubes

demonstrated a salt-removal capacity of 13.11 mg g⁻¹ and an outstanding salt-removal efficiency of 89.6% in a 500 mg L⁻¹ NaCl solution. The variable electrochemical performances of various TiO₂ polymorphs with distinctive open structures directly affect the desalination results. According to density functional theory (DFT), anatase TiO₂ creates 2D ion diffusion channels along both the *a*- and *b*-axes, which are distinguished by considerably reduced sodiation energy barriers³³. Meanwhile, rutile TiO₂ only offers one ion diffusion channel along the *c*-axis. This suggests that compared to the rutile phase, anatase TiO₂ more easily facilitates sodium-ion movement. A variety of TiO₂@porous carbon (TiO₂@PC) composites with various phases, including anatase, rutile, and mixed phases, were prepared by Ding et al.²⁵ in a comparative experiment by varying the annealing temperature. The resultant composites demonstrated improved salt-removal capacity for composites produced at lower thermal treatment temperatures; at 10 mA g⁻¹ in a 1000 mg L⁻¹ NaCl solution, the anatase TiO₂ electrode annealed at 600 °C demonstrated a higher salt-removal capacity (46.7 mg g⁻¹) than those of the mixed-phase TiO₂ electrode annealed at 800 °C (41 mg g⁻¹) and rutile TiO₂ electrode annealed at 1000 °C (34.4 mg g⁻¹). These results emphasize the superior sodium-ion movement in the anatase phase to that in the rutile phase. Strong annealing and harsh conditions are required to activate the TiO₂ to improve its efficiency for salt removal. The 2D sheets of TiO₂ can be proved highly effective in the intercalation and deintercalation of ions on demand; however, the synthesis of 2D sheets of TiO₂, such as star graphene-like materials, is challenging. We believe that finding high-quality 2D TiO₂ sheets will be revolutionary in materials chemistry science and that a new race can begin by utilizing 2D sheets of TiO₂ for various applications.

Herein, we present an advanced process for synthesizing high-quality graphene-like 2D TiO₂ nanosheets using a simple and cost-effective air-gap-assisted solvothermal approach. Notably, we could control the 2D sheets and TiO₂ phase by simply tuning the free space inside the solvothermal reactor. Herein, we successfully revealed that by simply varying the air-gap in the container, perfect 2D TiO₂ sheets that appear similar to graphene can be produced, and by varying the gap, the crystallinity of the 2D sheets of TiO₂ can be increased. After air-gap optimization, 2D sheets of the anatase TiO₂ phase with high crystallinity were obtained. The obtained material was used as a Faradaic electrode in ion-electrosorption-based technologies for possible utilization in CDI to desalinate water. Examination of the electrochemical performance of the 2D TiO₂ electrode revealed its good electrochemical stability and desalination performance. Because of its layered structure, 2D TiO₂ has more active adsorption sites and surface defects and shorter ion diffusion routes. Based on the electrochemical conductivity, Na⁺ migration and storage were investigated in situ. This study proposes a method for synthesizing a wrinkled graphene-like 2D TiO₂, which exhibits excellent electrochemical desalination properties.

Results and discussion

TiO₂ exists in three main crystal structures: anatase, rutile, and brookite. The XRD pattern for each phase is distinctive, with characteristic peaks corresponding to the atomic arrangement in each crystal structure. Anatase TiO₂ has a tetragonal crystal structure with lattice parameters *a* = 3.785 Å and *c* = 9.514 Å, and its XRD pattern is characterized by sharp peaks at 2θ = 25.3°, 37.8°, 48.1°, 54.0°, and 62.7°. Rutile TiO₂ has a tetragonal crystal structure with lattice parameters *a* = 4.594 Å and *c* = 2.958 Å, and its XRD pattern is characterized by sharp peaks at 2θ = 27.5°, 36.1°, 41.2°, 54.3°, 56.6°, and 69.1°. Brookite TiO₂ has an orthorhombic crystal structure with lattice parameters *a* = 5.517 Å, *b* = 9.181 Å, and *c* = 5.149 Å, and its XRD pattern is characterized by sharp peaks at 2θ = 26.1°, 37.9°, 39.6°, 41.0°, 49.3°, 54.5°, and 64.0°³⁴. Figure 1a depicts the XRD pattern of the four prepared TiO₂ materials under different conditions. The primary diffraction peaks of the synthesized materials were found to match the anatase phase of TiO₂; that is, the (101), (004), (200), and (211) crystal faces of anatase TiO₂ are represented by four diffraction peaks at 2θ of 25.8°, 37.7°, 47.8°, and 55.0°^{35,36}. Furthermore, the absence of diffraction peaks at 27° or 31° suggests that the samples are not contaminated by rutile or brookite impurities³⁷. As can be

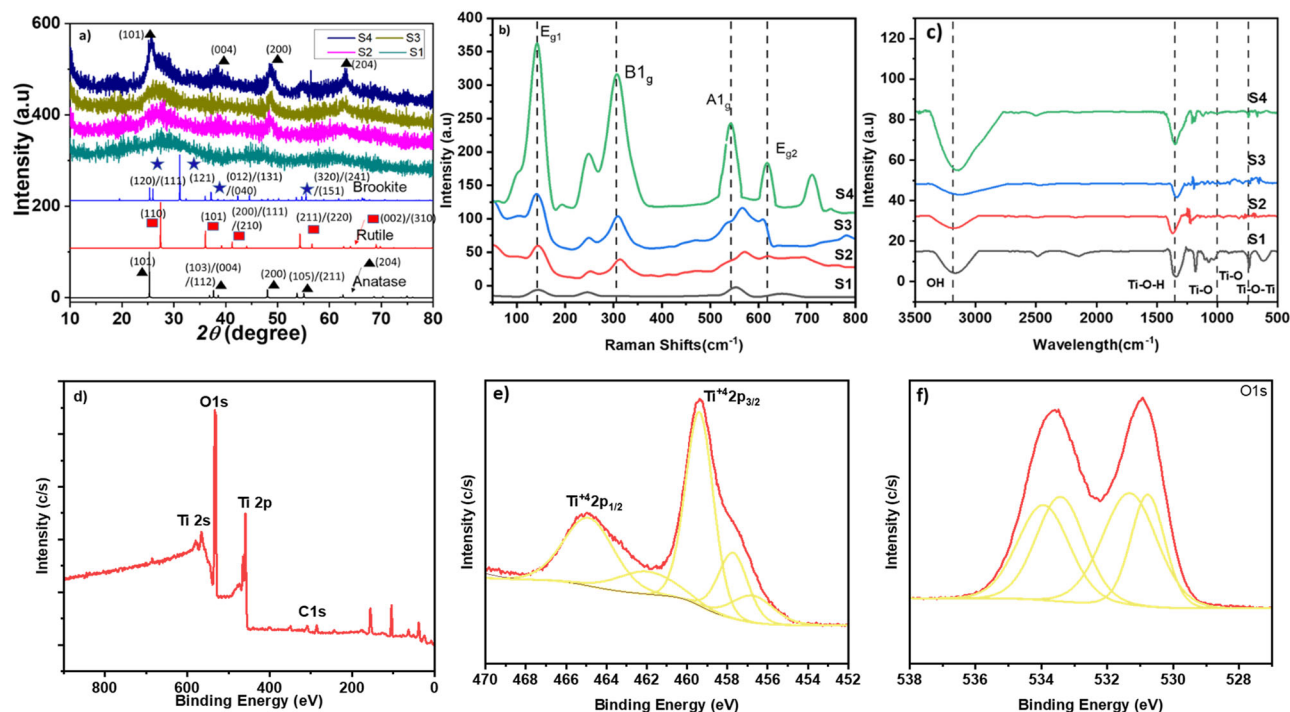


Fig. 1 | Structural characterization of the synthesized 2D TiO₂ sheets. a XRD patterns, **b** Raman spectra, **c** Fourier transform-infrared (FTIR) spectra, **d** XPS survey spectra of TiO₂, and high-resolution spectra of **e** Ti 2*p* and **f** O 1*s*.

concluded based on comparison with the standard pattern of anatase TiO₂ (JCPDS no. 21-1272), the samples synthesized under various conditions were entirely composed of a pure anatase phase. In addition, the peak intensity related to samples S1, S2, S3, and S4 increased by increasing the air-gap during solvothermal synthesis; the anatase peak (at 25.8°) was sharper for sample S4 than for the other samples, and the sharpness increased from S1 to S4, thereby confirming the increase in the 2D TiO₂ sheet crystallinity. Moreover, the average crystallite size of the S4, estimated by the Scherrer and the Williamson-Hall models, was 1.33 and 2.01 nm, respectively, confirming the nano-crystallinity of the synthesized materials.

Raman spectroscopy was used to evaluate and confirm the structure of the synthesized 2D materials. The Raman spectrum of TiO₂ exhibits several prominent peaks that can be assigned to specific vibrational modes (Fig. 1b). The peak at approximately 144 cm⁻¹ is known as the E_g mode and is associated with the symmetric stretching of Ti-O bonds in the crystal lattice. The peak at approximately 386 cm⁻¹ is known as the B1_g mode and is associated with the bending of Ti-O-Ti bonds. The peak at approximately 519 cm⁻¹ is known as the A1_g mode and is associated with the symmetric stretching of Ti-O bonds. The peak at approximately 631 cm⁻¹ is known as the E_g mode and is associated with the symmetric bending of Ti-O bonds. Interestingly, these peaks are characteristic of anatase TiO₂^{38–40}. The Raman spectra are consistent with the results obtained by XRD, with the intensity of the characteristic peak of the anatase phase at 144 increasing from S1 to S4 and thus confirming that our air-gap protocol used in preparing the TiO₂ nanosheets allows the control of their crystallinity. The Raman spectrum of TiO₂ provides valuable information regarding its crystal structure, phase purity, and defects. Anatase is one of the three naturally occurring crystal structures of TiO₂ and has unique properties, such as its high surface area, low energy barrier for ion insertion, and two-dimensional intercalation path, that make it suitable for electrochemical desalination.

In the FTIR spectrum of TiO₂ (Fig. 1c), several key bands are important for identifying the material. These bands originated from the vibrational modes of the Ti-O bonds in the crystal lattice. The resulting spectrum provided information on the vibrational modes of the sample. O-H stretching is detected at approximately 1623 and 3400 cm⁻¹, indicating that the material is hydroxylated. Ti-O stretching is indicated by vibration that

occurs at approximately 600–800 cm⁻¹ and is ascribed to the stretching of the Ti-O bond in the anatase structure. Ti-O bending is characterized by the vibration that occurs at approximately 400–500 cm⁻¹ and is attributed to the bending of the Ti-O bond in the anatase structure⁴¹; notably, no prominent additional vibrational peaks that can be associated with the air-gap-assisted solvothermal conditions are observed; all samples exhibit the same vibrational peaks with minimal difference in peak intensity.

X-ray photoelectron spectroscopy (XPS) is a powerful analytical technique that provides information on the chemical state and composition of a material surface⁴². The XPS survey spectra of the TiO₂ thin films are presented in Fig. 1d, which shows that the presence of the carbon peak is most likely due to instrument impurities. Figure 1e shows a high-resolution XPS spectrum of pure TiO₂ film; the Ti 2*p* XPS spectrum displays two peaks at 458.36 and 464.88 eV, which are attributed to Ti⁴⁺. The area ratio between these peaks is 2:1, which is stoichiometrically consistent. The difference in binding energy between the Ti 2*p*_{3/2} and Ti 2*p*_{1/2} peaks is 5.45 eV, which agrees with the known values for Ti⁴⁺-O bonding in TiO₂^{43,44}. Additionally, the shoulder Ti 2*p*_{1/2} at the binding energy of 461.98 eV corresponds to the oxidation state Ti³⁺ in Ti₂O₃^{45–47}. These findings suggest that the film generates both TiO₂ and Ti₂O₃ during its formation. The presence of Ti³⁺ can be attributed to the oxygen vacancies generated by our unique method, which consists of the variation in air-gap during the solvothermal process; the oxygen vacancies are generated by the calcination temperature⁴⁸ and air plasma treatment⁴⁵.

The O 1*s* spectrum displays two peaks at 530.77 and 533.42 eV, which are associated with the lattice and non-lattice oxygens of TiO₂, respectively (Fig. 1f)⁴⁹. The binding-energy difference between the Ti 2*p*_{3/2} peak and the O 1*s* lattice oxygen peak is 72.7 eV, which is close to that observed for anatase TiO₂ (71.4 eV)^{47,50}. These results provide important information regarding the chemical composition and bonding of TiO₂, which can be useful for understanding its properties and potential applications. The relative peak areas of the lattice and non-lattice oxygen peaks provide information regarding the surface structure of the material, with the majority of oxygen atoms being in the lattice sites. The similarity between the binding-energy differences observed for TiO₂ and anatase TiO₂ suggests that the material has a surface structure and bonding environment similar to

that of anatase TiO₂. Notably, the inclusion of oxygen vacancies naturally improves the electrical conductivity of the 2D TiO₂@CP electrode, which is beneficial for advanced sodium storage. In addition, this approach is effective for enhancing the capacity and cyclability of other electrochemical energy systems based on metal oxides^{51–53}.

TEM showed the remarkable transformation of TiO₂ into 2D sheets as the air gap in the solvothermal autoclave was varied (Fig. 2a–d). As evidently seen in the TEM images, the resulting nanosheets prepared with various air gaps exhibited a 2D-layered structure with different ranges of crystallinity. The TiO₂ sheets started turning from multiple layers to a few or ultrathin layers. Figure 2 shows that the thickness of the TiO₂ nanosheets is in the range of atomic dimensions, whereas their lateral dimensions are in the range of micrometers. However, the TEM image (Fig. 2a) shows the low crystallinity of the pristine TiO₂ nanosheets, given that the lattice fringes are not clearly visible and as confirmed by a diffraction spot (inset Fig. 2a). S1, TiO₂ was synthesized simply by heating in an open atmosphere at 80 °C. The TiO₂ appeared multilayer, and most of it was amorphous and lacked crystallinity, as was evident from the selected-area electron diffraction (SAED) and XRD patterns of S1 TiO₂. The morphology of TiO₂ completely changed when the air-gap-assisted solvothermal process was adopted to synthesize the material. Figure 2b–d illustrates the effects of different air gaps on the structure and crystallinity of the TiO₂ nanosheets. As the air gap in the reactor increased, the 2D nanosheets gradually became crystalline. The sheet-like structure of TiO₂ was recognizable in all air-gap-assisted solvothermal syntheses. Figure 2d shows the TiO₂ nanosheet prepared at a larger air gap, which has a thin, paper-like appearance and is characterized by a high number of wrinkles; this appearance is similar to that of the graphene nanosheet⁵⁴. To the best of our knowledge, these are unprecedented 2D sheets of TiO₂, not observed previously; notably, the air-gap-assisted solvothermal method

can be used to produce these sheets in bulk. Thus, the TEM images confirm that the TiO₂ nanosheets have a two-dimensional shape and a layered structure.

HRTEM analysis of sample S4 (Fig. 3) reveals that the lattice fringes have an inter-layer distance of 0.346 nm, which approximately correlates to the lattice spacing of the (101) planes of anatase TiO₂, which is 0.351⁵⁵. The (200) planes of anatase TiO₂ could be identified by a lattice spacing of approximately 0.189 nm, whereas a lattice spacing of approximately 0.235 nm corresponds to the (001) planes of anatase TiO₂⁵⁶. This observation is consistent with the XRD study results. The results of TEM and SAED analyses show that varied free spaces affect not only the crystalline phase and crystallinity of the TiO₂ nanostructures but also their morphologies. Anatase TiO₂ is a suitable material for Na electroadsorption because of its high surface area, unique surface chemistry, and good electrochemical stability. The presence of the {001} and {200} facets in anatase TiO₂ nanosheets can provide a high density of surface sites for Na adsorption, which can enhance electrochemical performance for sodium-ion storage. Additionally, anatase TiO₂ exhibits a reversible intercalation/deintercalation of sodium ions, making it a promising candidate for use in sodium-ion batteries^{57,58} and meanwhile, the surface area analysis of the pristine (S1) and the air-gap-assisted crystalline (S4) nanosheets was conducted and presented in Fig. 4a. The N₂ adsorption isotherms of both materials at 77 K indicate that S1 exhibits microporous features, while S4 has resulted in an extensive increase in mesoporosity as depicted by the hysteresis loop on the BET isotherm due to the air-gap solvothermal synthesis of S4. The corresponding increase in N₂ uptake on S4 further confirms the layering of the 2D nanosheets and the increase in the inter-layer spacing. Consequently, the BET surface area of S1 was estimated at 249.5 m²/g, while S4 has a value of 934.5 m²/g. Furthermore, the pore size distribution estimated by the non-linear DFT method (Fig. 4b) revealed that S4 has an average pore size of 0.60 nm, in contrast to

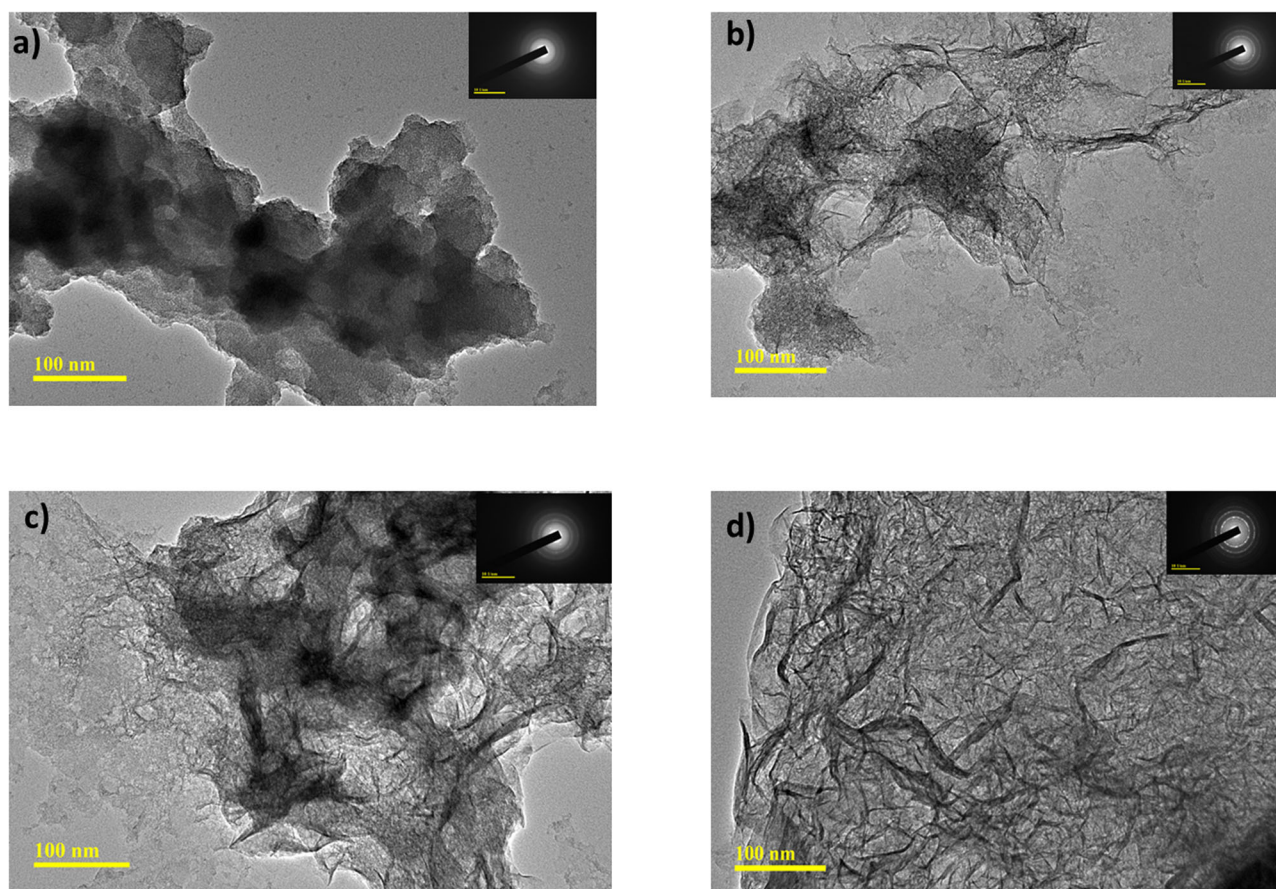


Fig. 2 | Morphological analysis of the synthesized 2D TiO₂ sheets. Transmission electron microscopy (TEM) images of the synthesized 2D TiO₂ sheets a S1, b S2, c S3, d S4 under atmospheric and various air-gap-assisted solvothermal conditions.

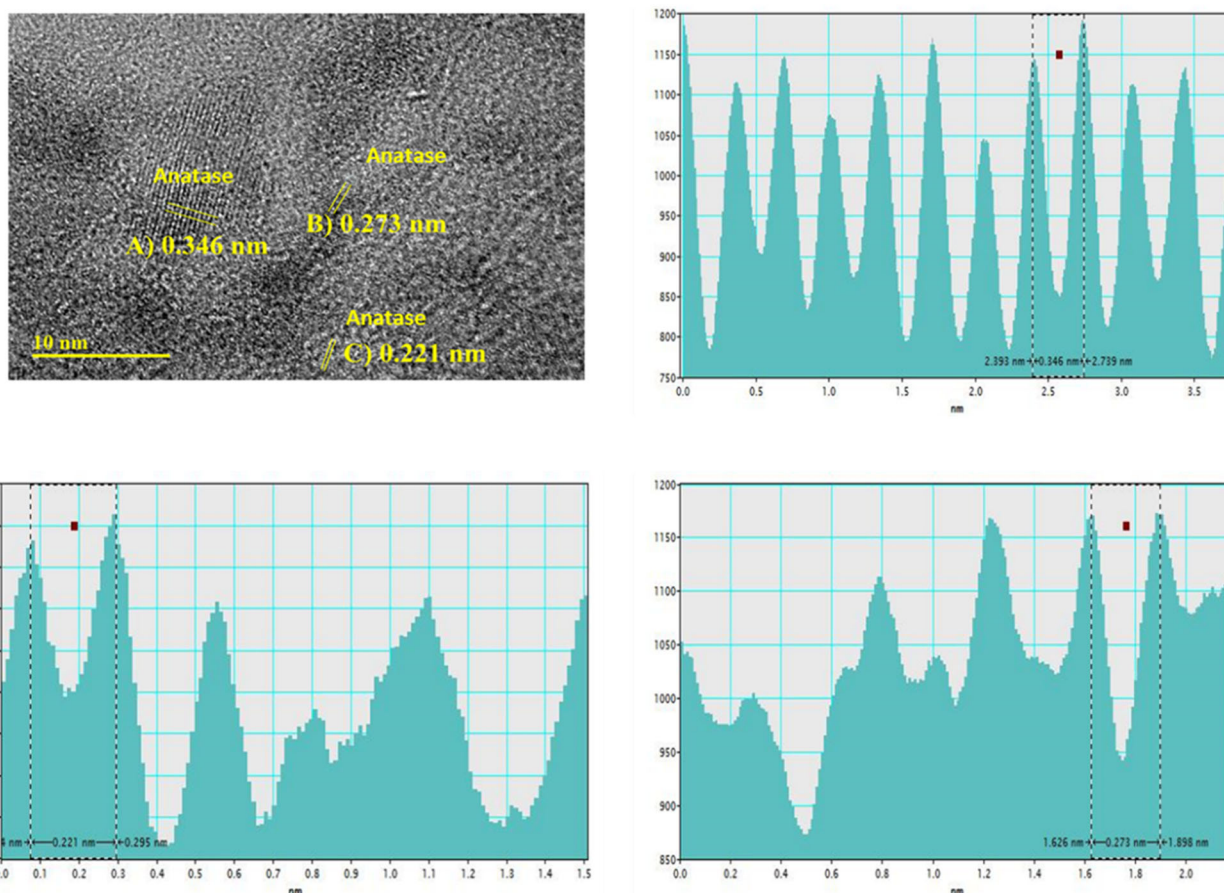


Fig. 3 | High-resolution TEM lattice fringes of 2D TiO₂. High-resolution TEM lattice fringe images of the 001 plane corresponding to anatase TiO₂.

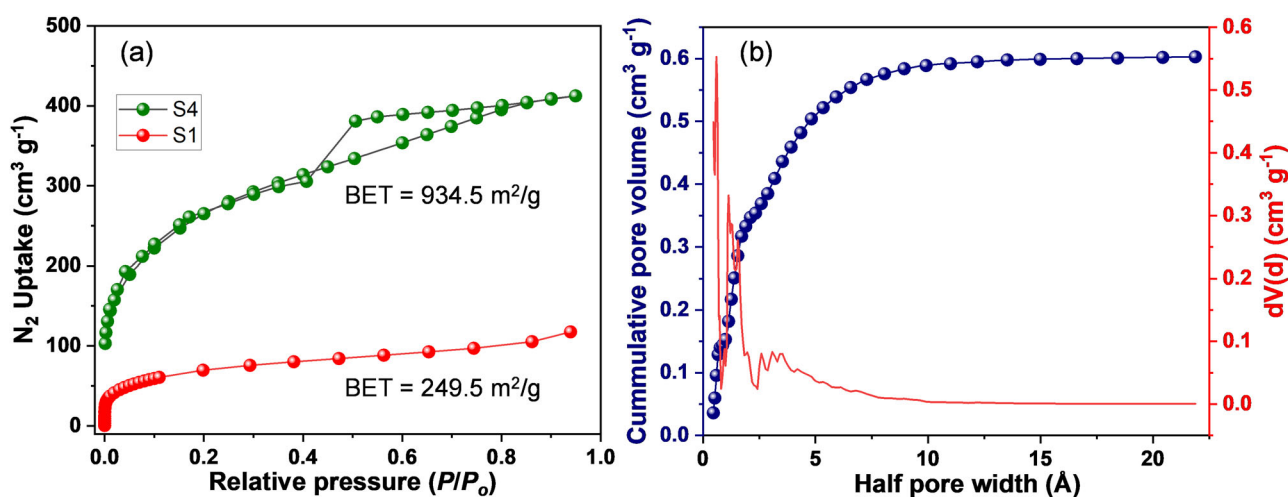


Fig. 4 | BET surface area and pore size distribution of 2D TiO₂. **a** N₂ sorption isotherms of S1 and S4 at 77 K, and **b** the pore size distribution of S4 estimated by the non-linear DFT method.

the 0.02 nm recorded for S1, making S4 a potential material for the efficient electro sorption of Na⁺ ions.

Electrochemical study

All electrochemical measurements were performed in a 1.0 M NaCl aqueous solution using a three-electrode setup consisting of a platinum counter electrode, Ag/AgCl reference electrode, and 2D TiO₂@CP working electrode. The 2D TiO₂@CP CV curves (Fig. 5a) show quasi-rectangular geometries with no evident redox peaks within the potential range ranging from

0.2 V to 0.8 V. The broad redox peaks shown at 0.3 and 0.4 V correspond to the insertion/de-insertion of Na⁺ based on the redox couple Ti⁴⁺/Ti³⁺⁵⁹. We believe that during the CV scans and owing to the layered structure of the material, sodium titanate was formed. Sodium titanates are a family of chemical compounds containing Na and titanium oxide (TiO_x) in various stoichiometries. They exhibit a layered crystal structure consisting of alternating sheets of titanium oxide (TiO₆) and sodium ions. This architectural design generated accessible tunnels along the *b*-axis, thereby facilitating Na⁺ diffusion⁶⁰. Fig. 5b shows a CV scan at 10 mV/s for the 2D

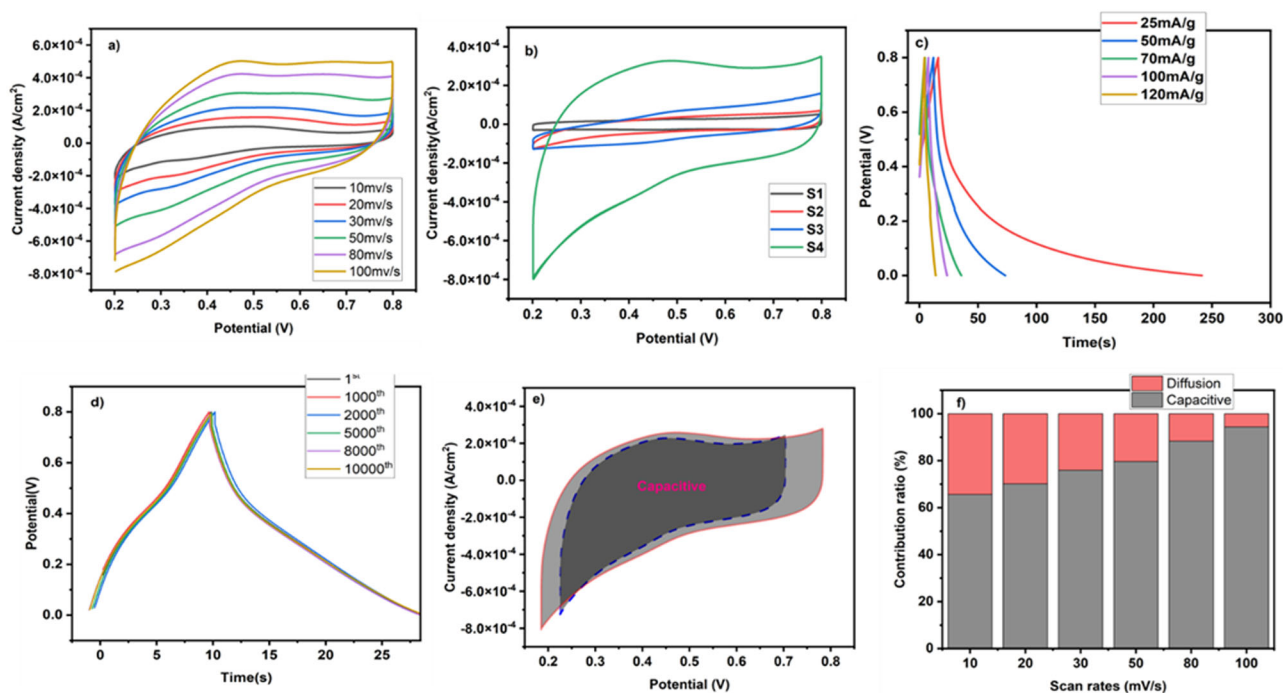
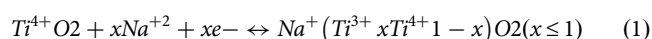


Fig. 5 | Electrochemical characterizations of 2D TiO₂. Cyclic voltammetry (CV) curves of 2D TiO₂ at **a** different scan rates and **b** under different preparation conditions; **c** galvanostatic charge–discharge (GCD) profiles at different specific current

densities, **d** GCD curves from the first to 10000th cycle at a specific current of 100 mA g⁻¹ **e** capacitive and diffusion contributions at 100 mV s⁻¹ and **f** contribution ratio of capacitive capacities at different scan rates.

fabricated electrodes. For the TiO₂ nanosheets prepared under different conditions (S1, S2, S3, and S4), all of the CV curves show quasi-rectangular geometries with no evident redox peaks within a potential range of 0.2–0.8 V. Equation (7) was used to calculate the specific capacity from the CV scan of the different materials; the specific capacity of the electrode fabricated with S4 was higher than that of the electrode fabricated using materials S1, S2, and S3, with specific capacities of 4.993, 6.881 and 7.875 F g⁻¹, respectively; by comparison, that of S4 was estimated to be 45.68 F g⁻¹. This confirms the high performance of S4 because of its high surface area, unique surface chemistry, and good electrochemical stability. Anatase TiO₂ is a suitable material for sodium electrosorption. Anatase TiO₂ nanosheets with {001} and {200} facets have a high density of surface sites for sodium adsorption, which can enhance electrochemical performance for sodium-ion storage.

2D TiO₂@CP demonstrated superior capacitive performance when the scan rate was varied from 10 mV s⁻¹ to 100 mV s⁻¹ because of its enhanced enclosed area provided by its CV curve. As shown above, at a scanning rate of 10 mV s⁻¹, the specific capacitance of 2D TiO₂@CP was approximately 49.43 mA h g⁻¹, and its shape remained stable as the scanning speed increased. The GCD measurements in a 1 M NaCl solution did not reveal any distinct redox platform, suggesting that the 2D TiO₂@CP electrode is a pseudocapacitive Faradaic electrode material, implying that the Faradaic phenomenon occurs on or near the surface of the electrode material (Fig. 5c)^{61,62}. The electrode exhibited outstanding performance and cycling stability in NaCl solution, with minimal changes in the specific capacity and retention rate even after 10000 cycles; these results demonstrate its high electrochemical stability in water (Fig. 5d). Consequently, the extraction of Na⁺ can be attributed to Faradaic and surface redox reactions, with the specific reaction Eq. 1 given as follows⁶³:



The EIS spectrum and CVs of 2D TiO₂ can be seen in Supplementary Figs. 1 and 2. The behavior of the 2D TiO₂@CP electrode material during the charge–discharge process was influenced by the redox reaction and ion

diffusion⁶². As demonstrated by performing tests at various scanning rates, the electrode material exhibited pseudocapacitive behavior owing to its small volume and large surface area. The *b* value calculated using Eq. (6) was 0.76, indicating that the redox reaction is controlled by ion diffusion (inset of Fig. 5e). To determine the respective contributions of diffusion-controlled and pseudocapacitive behavior to the total sodium storage, Eq. 2 is used:

$$i(v) = k_1v + k_2v^{1/2} \quad (2)$$

where *i*(*v*), *k*₁*v*, and *k*₂*v*^{1/2} denote the total capacitive-controlled, and diffusion-controlled currents, respectively. To obtain the constants *k*₁ and *k*₂, the *i*(*v*)/*v*^{1/2} – *v*^{1/2} plots of the CV curves at different scan rates were linearly fitted. Quantitative analyses revealed that at a scan rate of 100 mV s⁻¹, the pseudocapacitance contribution to the total Na⁺ storage was 94%, whereas the contribution of diffusing charge was only 6% (Fig. 5e), corresponding to Na⁺ intercalation/deintercalation in the anatase TiO₂ nanosheets^{64,65}. Most of the ion storage occurred on the surface of the two-dimensional TiO₂ nanosheets⁶². As the scanning rate decreased, the diffusion contribution increased whereas the capacitance contribution decreased, as shown in Fig. 5f. At 10 mV s⁻¹, the capacitance contribution of the 2D TiO₂@CP electrode was 65% of its total capacity, suggesting that the electrode material has promising applications in pseudocapacitive sodium storage and electrosorption–desalination.

Adsorption/desorption of Na⁺ ions on the TiO₂ composite film

A three-electrode configuration was used at room temperature to examine the electrosorption–desalination performance of the 2D TiO₂/CP electrodes. Figure 6a illustrates the trend of conductivity versus time. Evidently, the conductivity decreased when the negative potential was applied, thus confirming the adsorption of Na⁺ ions during the charging process. During the discharging phase, Na⁺ ions were desorbed from the electrolyte, resulting in an increase in conductivity^{27,28}. A reversible reaction occurred during discharge, releasing Na⁺ and Cl⁻ into the electrolyte and increasing the electrical conductivity⁶⁶. Furthermore, the 2D TiO₂/CP electrode exhibited good electrosorption–desalination performance stability after six cycles without

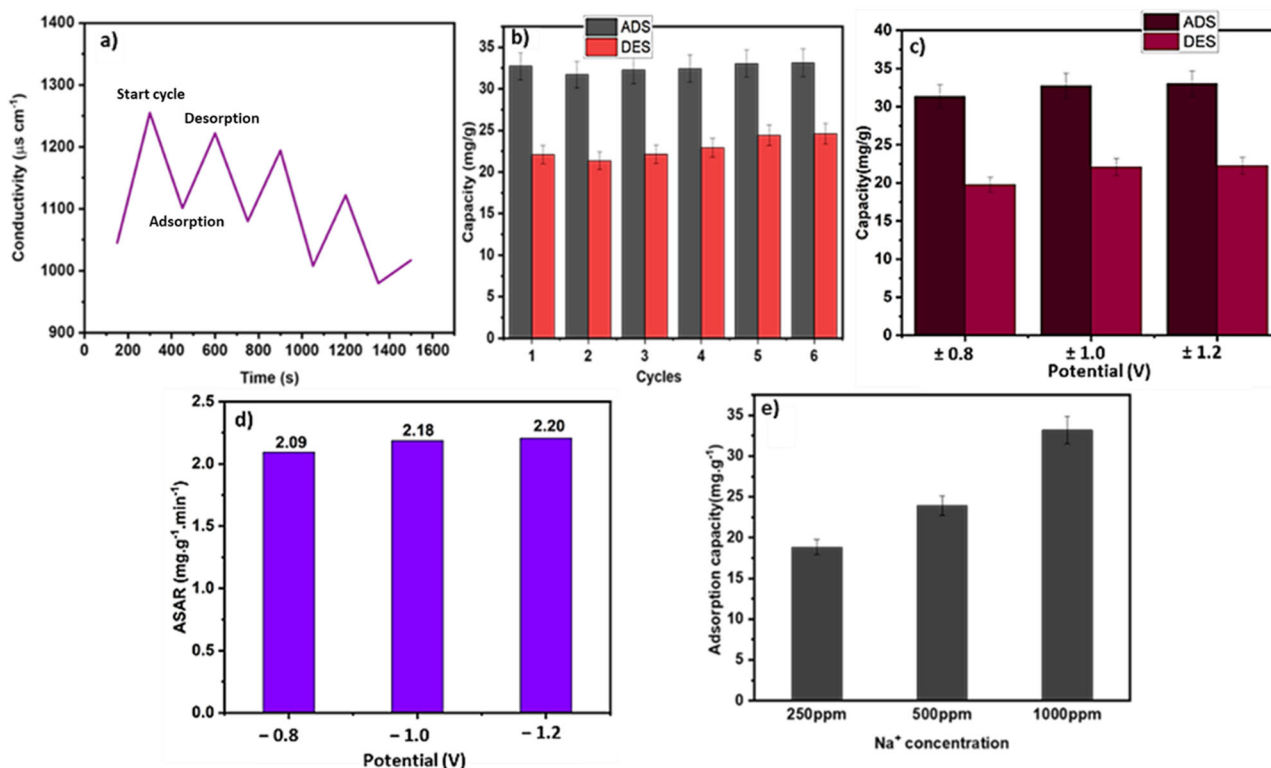


Fig. 6 | Adsorption and desorption of Na⁺ ions on the 2D TiO₂ electrodes. Trends of a conductivity fluctuation, b long-term salt adsorption capacity, c and salt adsorption capacity (SAC) at different cutoff voltage ranges; d salt adsorption rate of

2D TiO₂ at different cutoff voltage ranges, and e SAC at different Na⁺ concentrations. The error bars on the graphs demonstrate the standard deviation within two sets of data.

Table 1 | Comparisons between the desalination capacities of different types of electrodes

Material	Salt adsorption capacity (mg g ⁻¹)	Specific capacity (F g ⁻¹)	Concentration	References
Coconut-shell activated carbon (AC)	9.15	112		69
AC particle electrode modified by phosphoric acid	15.52	-	500 mg L ⁻¹	70
3D-Na ⁺ -Ti ₃ C ₂ T _x	16.2	143.2	100 mg L ⁻¹	71
Graphene/CNTs/ZnO (FGC-ZnO)	28.62	280	600 mg L ⁻¹	72
ZIF-8-derived polyhedron particles	8.52	160.8	1 M	73
Nitrogen-TiO ₂ /ZrO ₂ nanofibers incorporated AC (NACTZ)	3.98	691.78		74
MoS ₂ /CNT	25	75	500 mM	75
2D-layered TiO ₂	33.19	45.68	1000 mg L ⁻¹	This work

any substantial decline (Fig. 6b). The desalination capacity of the 2D TiO₂/CP electrode was 33.19 mg g⁻¹ as determined using Eq. (3). To study the effects of various applied potentials, electrosorption–desalination tests were carried out on the 2D TiO₂/CP electrode using a three-electrode setup using a solution with a NaCl concentration of 1,000 mg L⁻¹. The applied potentials for the 2D TiO₂/CP electrodes were in the ranges of 0.8 to -0.8, 1.0 to -1.0, and 1.2 to -1.2 V, respectively, and the adsorption time was fixed at 15 min. Various applied potential ranges for SAC are shown in Fig. 6c. The average adsorption capacity values for -0.8 V, -1.0 V, and -1.2 V were 31.33, 32.73, and 33.023 mg g⁻¹, respectively, indicating that the adsorption capacity increases with increasing applied potential. Meanwhile, the typical salt adsorption rates were 2.09, 2.18, and 2.20 mg g⁻¹ min⁻¹ at the same applied potential (Fig. 6d). The same trend was observed: the ASAR increased proportionally with the applied potential because driving forces of the Na⁺ and Cl⁻ ions increased under stronger electric fields at higher voltages, resulting higher ASARs^{66–68}. In addition, we performed the electrosorption process at different initial NaCl concentrations, and the results showed that the increase in the initial NaCl concentration led to the increase

in adsorption capacity; as seen in Fig. 6e, the SAC values were 18.81, 23.95, and 33.19 mg g⁻¹ for the initial Na⁺ concentrations of 250, 500, and 1000 ppm, respectively. Even at low NaCl concentration (250 ppm), an acceptable adsorption capacity can be achieved. Thus, 2D TiO₂ produced by the air-gap-assisted solvothermal process was highly activated to desalinate water from low-salt to high-salt-containing water, thus making it a multi-purpose electroactive material.

Interestingly, the electrode constructed using 2D TiO₂ exhibited superior desalination capacity to those of other comparable electrodes (Table 1), which may be due to the synergistic effect of the lamellar structure, shorter ionic diffusion path, more active adsorption sites, and pseudocapacitive behavior. Furthermore, compared with other materials, this unique 2D-layered TiO₂ had a larger desalination capacity and lower specific capacity. Compared with closed materials, a higher SAC for a smaller specific capacitance indicates a higher usage efficiency of our unique layered 2D TiO₂ material.

In summary, we introduced an air-gap-assisted solvothermal method to produce high-quality 2D TiO₂ material. The dimensions and crystallinity

of the sheets can be tuned by varying the air gap in the autoclave, and optimum tuning results in the formation of high-quality 2D sheets. The 2D TiO₂ possesses a layered structure that provides a multitude of active adsorption sites, surface defects, and shorter routes for ion diffusion. The remarkable electron-transfer rate and conductivity highlight the tremendous potential of this material for use in capacitive deionization applications. Notably, the electrode exhibited an impressive desalination capacity of 33.19 mg g⁻¹. These remarkable achievements can be attributed to the synergistic effects arising from the unique layered structure, large specific surface area, short ionic diffusion path, and pseudocapacitance of the material. The air-gap-assisted synthesis of high-quality 2D TiO₂ sheets described herein has potential applications in electro-storage, electro-catalysis, photocatalysis, and self-cleaning membranes.

Methods

Materials

Titanium(IV) isobutoxide was purchased from Sigma–Aldrich. Analytical reagent-grade dimethylformamide (DMF, 99.5%) was purchased from Fisher Scientific. Methanol was obtained from Scharlau. Sulfuric acid (H₂SO₄, 98%), hydrochloric acid (HCl), and sodium chloride (NaCl) solutions were obtained from Sigma–Aldrich and used as received.

Synthesis of 2D-layered TiO₂ nanosheets

Titanium(IV) isobutoxide was used as a precursor to synthesize various 2D sheets of TiO₂. In the first stage, titanium(IV) isobutoxide (2 g) was added to DMF (27 mL) and heated at 80 °C. The TiO₂ that was not further processed at this stage was denoted by S1. S1 (TiO₂) was the material that was obtained after 30 min of heating at 80 °C. Subsequently, three types of available solvothermal autoclaves, which had different air gaps or free volumes, were used after the addition of the precursors. The heated titanium(IV) isobutoxide in DMF was transferred into the solvothermal autoclave and kept for 48 h at 150 °C. The autoclave was then cooled to room temperature (25 °C). Subsequently, the obtained 2D TiO₂ sheets were collected by centrifugation at 6000 rpm and cleaning by washing several times with methanol. The 2D TiO₂ sheets were called S2, S3, and S4, in accordance with the air-gap or free volume of the PTFE autoclaved reactor container of 25, 50, and 250 mL, respectively. 18 mL of the precursor-containing solution was transferred into a 25 mL container. The air gap during the synthesis increased with the distance from S2 to S4.

Fabrication of TiO₂/CP electrode

The as-prepared 2D TiO₂ sheets were dispersed in DMF and then poured directly onto the surface of carbon paper (CP). Thereafter, the mixture was dried at 60 °C for 12 h. TiO₂ adhered uniformly to the CP without the need for a binder. The prepared electrode was referred to as 2D TiO₂@CP.

Characterization

X-ray diffraction (XRD) (Malvern Panalytical X'Pert3) was used to examine the TiO₂ nanosheet and electrode structures. The analyses were performed at a scanning rate of 0.04 °C/min in the 5–70° range. A field-emission transmission electron microscopy (FE-TEM) system (JEOL JEM2100F) was used to study the morphologies and structures of the samples. The Fourier transform-infrared (FTIR) spectra of the TiO₂ nanosheets were recorded using a Thermo Scientific Nicolet Is5 instrument in the range of 500–4000 cm⁻¹.

Electrochemical measurements

Electrochemical characterization tests were performed using a multi-channel potentiostat (Corrtest CS 310), which was controlled using CS Studio6. A three-electrode setup was used to evaluate electrochemical performance. The counter electrode was a Pt mesh, and the reference electrode was Ag/AgCl. Using an electrochemical setup, the cyclic voltammetry (CV) curves of the electrodes were recorded in a 1 M aqueous NaCl solution in the potential range of 0.2–0.8 V (versus Ag/AgCl). Measurements were performed at scan rates of

100, 50, 30, 10, and 1 mV/s. Na extraction measurements were performed using a 60 mL electrolytic cell; the distance between the electrodes was maintained at 15 mm.

Three electrodes were used to test the electrochemical adsorption and desorption of Na⁺ onto the 2D TiO₂/CP electrode at room temperature. The amount of NaCl aqueous solution used in this experiment was 15 mL, and the Na⁺ ion concentration was maintained at 1000 ppm. 2D TiO₂/CP, Pt mesh, and Ag/AgCl electrodes were used as the working, counter, and reference electrodes, respectively. The working electrode was subjected to a reduction potential of –1 V for electrochemical adsorption of Na⁺ ions. Equation (3) was used to determine the adsorption capacities of the electrode films (Q):

$$Q = \frac{(C_o - C_e) \times V}{m} \quad (3)$$

where C_o and C_e represent the initial and final concentrations, respectively; V represents the volume of the aqueous solution; and m represents the mass of the TiO₂/CP hybrid film. After the TiO₂/CP hybrid film electrode adsorbed the Na⁺ ions, a voltage of 1.0 V was applied as the oxidation potential to achieve Na⁺ desorption.

The desorption ratio of the composite film was calculated using Eq. (4):

$$\text{Desorption ratio} = \frac{Q_s}{Q_e} \quad (4)$$

where Q_s represents the amount of Na⁺ ions desorbed into the solution and Q_e represents the amount of Na⁺ ions adsorbed by the 2D TiO₂/CP film.

The average salt adsorption rate (ASAR, mg g⁻¹ min⁻¹) was calculated based on Eq. (5)

$$\text{ASAR} = \text{SAC}/t \quad (5)$$

where SAC is the Salt Adsorption Capacity (mg g⁻¹) and t is the desalination time (min).

In general, the power-law relationship between the currents and scan speeds of the CV curves conforms to Eq. (6)

$$i = av^b \quad (6)$$

$$C_p = \frac{A}{2mK\Delta V} \quad (7)$$

where C_p is the specific capacitance in F g⁻¹, A is the area in AV, m is the material mass, K is the scan rate of CV in V s⁻¹, and ΔV the potential window of the CV. The error bars in the figures represent the standard deviation (SD).

Data availability

The main data that support the results of this study are available in this Article.

Received: 4 September 2023; Accepted: 29 January 2024;

Published online: 14 February 2024

References

- Shannon, M. A. et al. Science and technology for water purification in the coming decades. *Nature* **452**, 301–310 (2008).
- Urban, J. J. Emerging scientific and engineering opportunities within the water-energy nexus. *Joule* **1**, 665–688 (2017).
- AlMarzooqi, F. A., Al Ghaferi, A. A., Saadat, I. & Hilal, N. Application of capacitive deionisation in water desalination: a review. *Desalination* **342**, 3–15 (2014).

4. Kumar, S., Aldaqa, N. M., Alhseinat, E. & Shetty, D. Electrode materials for desalination of water via capacitive deionization. *Angew. Chem. Int. Ed.* **2023**, e202302180 (2023).
5. Klaysom, C., Cath, T. Y., Depuydt, T. & Vankelecom, I. F. J. Forward and pressure retarded osmosis: potential solutions for global challenges in energy and water supply. *Chem. Soc. Rev.* **42**, 6959–6989 (2013).
6. Elimelech, M. & Phillip, W. A. The future of seawater desalination: energy, technology, and the environment. *Science (1979)* **333**, 712–717 (2011).
7. Sadrzadeh, M. & Mohammadi, T. Sea water desalination using electrodialysis. *Desalination* **221**, 440–447 (2008).
8. Suss, M. E. et al. Water desalination via capacitive deionization: what is it and what can we expect from it? *Energy Environ. Sci.* **8**, 2296–2319 (2015).
9. Porada, S., Zhao, R., Van Der Wal, A., Presser, V. & Biesheuvel, P. M. Review on the science and technology of water desalination by capacitive deionization. *Prog. Mater. Sci.* **58**, 1388–1442 (2013).
10. Anderson, M. A., Cudero, A. L. & Palma, J. Capacitive deionization as an electrochemical means of saving energy and delivering clean water. Comparison to present desalination practices: Will it compete? *Electrochim. Acta* **55**, 3845–3856 (2010).
11. El-Deen, A. G. et al. TiO₂ nanorod-intercalated reduced graphene oxide as high performance electrode material for membrane capacitive deionization. *Desalination* **361**, 53–64 (2015).
12. Oren, Y. Capacitive deionization (CDI) for desalination and water treatment—past, present and future (a review). *Desalination* **228**, 10–29 (2008).
13. Burn, S. et al. Desalination techniques—A review of the opportunities for desalination in agriculture. *Desalination* **364**, 2–16 (2015).
14. Zinatloo-Ajabshir, S., Baladi, M. & Salavati-Niasari, M. Enhanced visible-light-driven photocatalytic performance for degradation of organic contaminants using PbWO₄ nanostructure fabricated by a new, simple and green sonochemical approach. *Ultrason. Sonochem.* **72**, 105420 (2021).
15. Huang, Z. H., Yang, Z., Kang, F. & Inagaki, M. Carbon electrodes for capacitive deionization. *J. Mater. Chem. A Mater.* **5**, 470–496 (2017).
16. Heydariyan, Z., Monsef, R. & Salavati-Niasari, M. Insights into impacts of Co₃O₄-CeO₂ nanocomposites on the electrochemical hydrogen storage performance of g-C₃N₄: Pechini preparation, structural design and comparative study. *J. Alloy. Compd.* **924**, 166564 (2022).
17. Amiri, M., Eskandari, K. & Salavati-Niasari, M. Magnetically retrievable ferrite nanoparticles in the catalysis application. *Adv. Colloid Interface Sci.* **271**, 101982 (2019).
18. Mir, N. & Salavati-Niasari, M. Preparation of TiO₂ nanoparticles by using tripodal tetraamine ligands as complexing agent via two-step sol-gel method and their application in dye-sensitized solar cells. *Mater. Res. Bull.* **48**, 1660–1667 (2013).
19. Amiri, M., Salavati-Niasari, M., Akbari, A. & Gholami, T. Removal of malachite green (a toxic dye) from water by cobalt ferrite silica magnetic nanocomposite: Herbal and green sol-gel autocombustion synthesis. *Int. J. Hydrog. Energy* **42**, 24846–24860 (2017).
20. Panahi-Kalamuei, M., Salavati-Niasari, M. & Hosseinpour-Mashkani, S. M. Facile microwave synthesis, characterization, and solar cell application of selenium nanoparticles. *J. Alloy. Compd.* **617**, 627–632 (2014).
21. Khojasteh, H., Salavati-Niasari, M., Safajou, H. & Safardoust-Hojaghan, H. Facile reduction of graphene using urea in solid phase and surface modification by N-doped graphene quantum dots for adsorption of organic dyes. *Diam. Relat. Mater.* **79**, 133–144 (2017).
22. Aravindan, V., Gnanaraj, J., Lee, Y. S. & Madhavi, S. Insertion-type electrodes for nonaqueous Li-ion capacitors. *Chem. Rev.* **114**, 11619–11635 (2014).
23. Yang, Z. et al. Nanostructures and lithium electrochemical reactivity of lithium titanites and titanium oxides: A review. *J. Power Sources* **192**, 588–598 (2009).
24. El-Deen, A. G., Choi, J. H., Khalil, K. A., Almajid, A. A. & Barakat, N. A. M. A TiO₂ nanofiber/activated carbon composite as a novel effective electrode material for capacitive deionization of brackish water. *RSC Adv.* **4**, 64634–64642 (2014).
25. Ding, M. et al. Tunable Pseudocapacitive Behavior in Metal-Organic Framework-Derived TiO₂@Porous Carbon Enabling High-Performance Membrane Capacitive Deionization. *ACS Appl. Energy Mater.* **2**, 1812–1822 (2019).
26. Chen, T., Wu, J., Zhang, Q. & Su, X. Recent advancement of SiOx based anodes for lithium-ion batteries. *J. Power Sources* **363**, 126–144 (2017).
27. Ramadan, M., Hassan, H. M. A., Shahat, A., Elshaarawy, R. F. M. & Allam, N. K. Ultrahigh performance of novel energy-efficient capacitive deionization electrodes based on 3D nanotubular composites. *N. J. Chem.* **42**, 3560–3567 (2018).
28. Yin, H. et al. Three-dimensional graphene/metal oxide nanoparticle hybrids for high-performance capacitive deionization of saline water. *Adv. Mater.* **25**, 6270–6276 (2013).
29. Liu, P. I. et al. Effects of activated carbon characteristics on the electrosorption capacity of titanium dioxide/activated carbon composite electrode materials prepared by a microwave-assisted ionothermal synthesis method. *J. Colloid Interface Sci.* **446**, 352–358 (2015).
30. Teymourinia, H., Salavati-Niasari, M., Amiri, O. & Safardoust-Hojaghan, H. Synthesis of graphene quantum dots from corn powder and their application in reduce charge recombination and increase free charge carriers. *J. Mol. Liq.* **242**, 447–455 (2017).
31. Heydariyan, Z., Monsef, R., Dawi, E. A. & Salavati-Niasari, M. EuMnO₃/EuMn₂O₅/MWCNT nanocomposites: Insights into synthesis and application as potential materials for development of hydrogen storage capacity. *Fuel* **351**, 128885 (2023).
32. Wei, K. et al. A novel capacitive electrode based on TiO₂-NTs array with carbon embedded for water deionization: fabrication, characterization and application study. *Desalination* **420**, 70–78 (2017).
33. Su, D., Dou, S. & Wang, G. Anatase TiO₂: better anode material than amorphous and rutile phases of TiO₂ for Na-ion batteries. *Chem. Mater.* **27**, 6022–6029 (2015).
34. Yang, X. H. et al. Ultra-thin anatase TiO₂ nanosheets dominated with {001} facets: thickness-controlled synthesis, growth mechanism and water-splitting properties. *CrystEngComm* **13**, 1378–1383 (2011).
35. Wang, C. et al. Hydrothermal growth of layered titanate nanosheet arrays on titanium foil and their topotactic transformation to heterostructured TiO₂ photocatalysts. *J. Phys. Chem. C.* **115**, 22276–22285 (2011).
36. Sharma, S. et al. Structural and photodetection studies of hydrothermally grown anatase TiO₂ nanomaterial. *Mater. Today Proc.* **73**, 255–262 (2023).
37. Xu, Y. et al. Nanocrystalline anatase TiO₂: a new anode material for rechargeable sodium ion batteries. *Chem. Commun.* **49**, 8973–8975 (2013).
38. Ohsaka, T., Izumi, F. & Fujiki, Y. Raman spectrum of anatase, TiO₂. *J. Raman Spectrosc.* **7**, 321–324 (1978).
39. Kavan, L. et al. Oxygen-isotope labeled titania: Ti₁₈O₂. *Phys. Chem. Chem. Phys.* **13**, 11583–11586 (2011).
40. Legrain, F., Malyi, O. & Manzhos, S. Insertion energetics of lithium, sodium, and magnesium in crystalline and amorphous titanium dioxide: a comparative first-principles study. *J. Power Sources* **278**, 197–202 (2015).
41. Al-Oubidy, E. A. & Kadhim, F. J. Photocatalytic activity of anatase titanium dioxide nanostructures prepared by reactive magnetron sputtering technique. *Opt. Quant. Electron* **51**, 1–11 (2019).

42. Carley, A. F., Chalker, P. R., Riviere, J. C. & Roberts, M. W. The identification and characterisation of mixed oxidation states at oxidised titanium surfaces by analysis of X-ray photoelectron spectra. *J. Chem. Soc., Faraday Trans. 1: Phys. Chem. Condens. Phases* **83**, 351–370 (1987).
43. Fu, Y. X. et al. TiO₂ nanorods anchor on reduced graphene oxide (R-TiO₂/rGO) composite as anode for high performance lithium-ion batteries. *Appl. Surf. Sci.* **497**, 143553 (2019).
44. Guo, X. et al. Porous TiB₂-TiC/TiO₂ heterostructures: synthesis and enhanced photocatalytic properties from nanosheets to sweetened rolls. *Appl. Catal. B* **217**, 12–20 (2017).
45. Bharti, B., Kumar, S., Lee, H. N. & Kumar, R. Formation of oxygen vacancies and Ti³⁺ state in TiO₂ thin film and enhanced optical properties by air plasma treatment. *Sci. Rep.* **6**, 1–12 (2016).
46. Bertóti, I., Mohai, M., Sullivan, J. L. & Saied, S. O. Surface characterisation of plasma-nitrided titanium: an XPS study. *Appl. Surf. Sci.* **84**, 357–371 (1995).
47. Biesinger, M. C., Lau, L. W. M., Gerson, A. R. & Smart, R. S. C. Resolving surface chemical states in XPS analysis of first row transition metals, oxides and hydroxides: Sc, Ti, V, Cu and Zn. *Appl. Surf. Sci.* **257**, 887–898 (2010).
48. Liu, G. et al. Role of the anatase/TiO₂(B) heterointerface for ultrastable high-rate lithium and sodium energy storage performance. *Nanoscale Horiz.* **5**, 150–162 (2019).
49. Chen, X. Q. et al. Fabrication of core-shell porous nanocubic Mn₂O₃@TiO₂ as a high-performance anode for lithium ion batteries. *J. Mater. Chem. A Mater.* **3**, 18198–18206 (2015).
50. Yu, J. C., Yu, J., Hung, Y. T. & Zhang, L. Effect of surface microstructure on the photoinduced hydrophilicity of porous TiO₂ thin films. *J. Mater. Chem.* **12**, 81–85 (2002).
51. Wu, N. et al. Anatase inverse opal TiO₂-x@N-doped C induced the dominant pseudocapacitive effect for durable and fast lithium/sodium storage. *Electrochim. Acta* **299**, 540–548 (2019).
52. Zhang, Y. et al. Oxygen vacancies evoked blue TiO₂(B) nanobelts with efficiency enhancement in sodium storage behaviors. *Adv. Funct. Mater.* **27**, 1700856 (2017).
53. Zhao, C. et al. Carbon-bonded, oxygen-deficient TiO₂ nanotubes with hybridized phases for superior Na-ion storage. *Chem. Eng. J.* **350**, 201–208 (2018).
54. Liu, C. et al. Fabrication and investigation on Ag nanowires/TiO₂ nanosheets/graphene hybrid nanocomposite and its water treatment performance. *Adv. Compos. Hybrid. Mater.* **3**, 402–414 (2020).
55. Li, L. et al. Visible light photochemical activity of heterostructured PbTiO₃-TiO₂ core-shell particles. *Catal. Sci. Technol.* **2**, 1945–1952 (2012).
56. Lee, M., Kim, M. S., Oh, J. M., Park, J. K. & Paek, S. M. Hybridization of layered titanium oxides and covalent organic nanosheets into hollow spheres for high-performance sodium-ion batteries with boosted electrical/ionic conductivity and ultralong cycle life. *ACS Nano* **17**, 3019–3036 (2023).
57. Wu, L., Buchholz, D., Bresser, D., Gomes Chagas, L. & Passerini, S. Anatase TiO₂ nanoparticles for high power sodium-ion anodes. *J. Power Sources* **251**, 379–385 (2014).
58. Wu, L. et al. Unfolding the mechanism of sodium insertion in anatase TiO₂ nanoparticle. *Adv. Energy Mater.* **5**, 1401142 (2015).
59. Kim, K. T. et al. Anatase titania nanorods as an intercalation anode material for rechargeable sodium batteries. *Nano Lett.* **14**, 416–422 (2014).
60. Senguttuvan, P., Rousse, G., Seznec, V., Tarascon, J. M. & Palacin, M. R. Na₂Ti₃O₇: Lowest voltage ever reported oxide insertion electrode for sodium ion batteries. *Chem. Mater.* **23**, 4109–4111 (2011).
61. Jiang, Y. & Liu, J. Definitions of pseudocapacitive materials: a brief review. *Energy Environ. Mater.* **2**, 30–37 (2019).
62. Yang, Z. et al. Two-dimensional hetero-structured TiO₂/TiS₂ nanosheets for capacitive deionization. *Chem. Mater.* https://doi.org/10.1021/ACS.CHEMMATER.2C03618/ASSET/IMAGES/LARGE/CM2C03618_0005.JPEG (2022).
63. Maça, R. R., Cíntora Juárez, D., Castillo Rodríguez, M. & Etacheri, V. Nanointerface-driven pseudocapacitance tuning of TiO₂ nanosheet anodes for high-rate, ultralong-life and enhanced capacity sodium-ion batteries. *Chem. Eng. J.* **391**, 123598 (2020).
64. Xu, H. et al. Controllable synthesis of anatase TiO₂ nanosheets grown on amorphous TiO₂/C frameworks for ultrafast pseudocapacitive sodium storage. *ACS Appl. Mater. Interfaces* **12**, 43813–43823 (2020).
65. Li, W. et al. A reversible phase transition for sodium insertion in anatase TiO₂. *Chem. Mater.* **29**, 1836–1844 (2017).
66. Liang, M., Bai, X., Yu, F. & Ma, J. A confinement strategy to in-situ prepare a peanut-like N-doped, C-wrapped TiO₂ electrode with an enhanced desalination capacity and rate for capacitive deionization. *Nano Res.* **14**, 684–691 (2021).
67. Li, H., Ma, Y. & Niu, R. Improved capacitive deionization performance by coupling TiO₂ nanoparticles with carbon nanotubes. *Sep. Purif. Technol.* **171**, 93–100 (2016).
68. Chang, L. M., Duan, X. Y. & Liu, W. Preparation and electrosorption desalination performance of activated carbon electrode with titania. *Desalination* **270**, 285–290 (2011).
69. Huynh, L. T. N. et al. Enhanced electrosorption of NaCl and nickel(II) in capacitive deionization by CO₂ activation coconut-shell activated carbon. *Carbon Lett.* **32**, 1531–1540 (2022).
70. Dou, C. et al. Chemical modification of carbon particles to enhance the electrosorption of capacitive deionization process. *J. Water Reuse Desalination* **10**, 57–69 (2020).
71. Chen, B. et al. High-performance capacitive deionization using 3D porous Ti₃C₂T_x with improved conductivity. *J. Electroanal. Chem.* **895**, 115515 (2021).
72. Arora, N., Banat, F., Bharath, G. & Alhseinat, E. Capacitive deionization of NaCl from saline solution using graphene/CNTs/ZnO NPs based electrodes. *J. Phys. D: Appl. Phys.* **52**, 455304 (2019).
73. Liu, N. L. et al. ZIF-8 derived, nitrogen-doped porous electrodes of carbon polyhedron particles for high-performance electrosorption of salt ions. *Sci. Rep.* **2016** **6**:1 **6**, 1–7 (2016).
74. Yasin, A. S., Mohamed, I. M. A., Mousa, H. M., Park, C. H. & Kim, C. S. Facile synthesis of TiO₂/ZrO₂ nanofibers/nitrogen co-doped activated carbon to enhance the desalination and bacterial inactivation via capacitive deionization. *Sci. Rep.* **2018** **8**:1 **8**, 1–14 (2018).
75. Srimuk, P. et al. Faradaic deionization of brackish and sea water via pseudocapacitive cation and anion intercalation into few-layered molybdenum disulfide. *J. Mater. Chem. A Mater.* **5**, 15640–15649 (2017).

Acknowledgements

This work was supported by the Interdisciplinary Research Center for Membranes and Water Security, King Fahd University of Petroleum and Minerals [grant number INMW2315].

Author contributions

B.S.: collected the data and performed the analysis, methodology, validation, and writing—the original draft. N.B.: conceptualization, designing materials, characterization, methodology, writing—review & editing. I.A.: characterization, interpretation, Writing—review & editing.

Competing interests

The authors declare no competing interests.

Additional information

Supplementary information The online version contains supplementary material available at <https://doi.org/10.1038/s41545-024-00304-x>.

Correspondence and requests for materials should be addressed to Nadeem Baig.

Reprints and permissions information is available at <http://www.nature.com/reprints>

Publisher's note Springer Nature remains neutral with regard to jurisdictional claims in published maps and institutional affiliations.

Open Access This article is licensed under a Creative Commons Attribution 4.0 International License, which permits use, sharing, adaptation, distribution and reproduction in any medium or format, as long as you give appropriate credit to the original author(s) and the source, provide a link to the Creative Commons licence, and indicate if changes were made. The images or other third party material in this article are included in the article's Creative Commons licence, unless indicated otherwise in a credit line to the material. If material is not included in the article's Creative Commons licence and your intended use is not permitted by statutory regulation or exceeds the permitted use, you will need to obtain permission directly from the copyright holder. To view a copy of this licence, visit <http://creativecommons.org/licenses/by/4.0/>.

© The Author(s) 2024